

# Damage analysis for an elastic-plastic body in cylindrical contact with a rigid plane



Bo Zhao <sup>a, b</sup>, Fei Shen <sup>b</sup>, Yi Cui <sup>c</sup>, Youbai Xie <sup>a</sup>, Kun Zhou <sup>b, \*</sup>

<sup>a</sup> State Key Laboratory of Mechanical System and Vibration, Shanghai Jiao Tong University, 800 Dongchuan Road, Minhang District, Shanghai, 200240, China

<sup>b</sup> School of Mechanical and Aerospace Engineering, Nanyang Technological University, 50 Nanyang Avenue, Singapore, 639798, Singapore

<sup>c</sup> Key Laboratory for Power Machinery and Engineering of Ministry of Education, Shanghai Jiao Tong University, 800 Dongchuan Road, Minhang District, Shanghai, 200240, China

## ARTICLE INFO

### Keywords:

Asperity contact  
Continuum damage mechanics  
Finite element analysis  
Elastic-plastic  
Kinematic hardening

## ABSTRACT

The fatigue failure can be explained by the accumulation of damage. By coupling the fatigue damage evolution with the elastic-plastic constitutive model, a numerical approach based on the continuum damage mechanics is proposed to conduct the fatigue damage analysis of the material under cyclic loadings. The elastic-plastic behavior of the material with nonlinear kinematic hardening effects and the damage induced by both cyclic stress and accumulated plastic strain are taken into account. The proposed approach is adopted to an asperity in cylindrical contact with a rigid flat under normal cyclic loading, which can be considered as a fundamental simplification of the contact between two rough surfaces. Finally, the fatigue macro-crack initiation and the evolution of load-carrying capacity of the asperity are predicted.

## 1. Introduction

The fixed joints, such as the bolted joints, play key roles in the overall static and dynamic characteristics of mechanical systems under static and dynamic loading. The experiments have shown that joints contribute much to the stiffness and damping in assemblies [1]. However, fretting fatigue damage easily occurs in contacting components and thus affects their proper function while they are subjected to fluctuated loading and relatively small movement [2]. On the microscopic scale, engineering surfaces are rough; primarily the asperities on the conjunction surfaces are in contact, which determines the stiffness of joints [3]. Therefore, it is very important to understand the damage mechanism of contacting asperities so as to predict the endurance and effectiveness of mechanical systems.

A single asperity contact pair with a rigid flat is generally considered as a fundamental simplification of the contact between rough surfaces [4]. In the past decades, many investigations on the asperity contact have been reported. Hertz [5] first conducted the elastic contact simulation without friction and adhesive. Greenwood and Williamson [6] applied the Hertz model to each asperity contact and developed the so-called GW contact model between complex surfaces. Then, by extending the GW model to the elastic-plastic contact, other scholars proposed several statistical elastic-plastic contact models [7,8].

Based on the finite element (FE) method, Kogut et al. [9] developed an elastic-plastic frictionless contact model (KE model) for a deformable sphere supporting a rigid flat. Jackson and Green [10] proposed the variations of the contact area and reaction force during the loading process. Shankar et al. [11] investigated the contact behavior of the material with different yield strengths and tangent moduli. With the aim of simulating granular materials using particle methods, Olsson and Larsson [12] presented a unified method for calculating the contact area and force between two dissimilar elastic-plastic spheres.

Besides the loading process considered above, the unloading process is equally important and should be also considered [13–15]. Etsion et al. [16] investigated the unloading performance of an elastic-plastic spherical contact. Kadin et al. [17] considered the adhesion behavior in the unloading process. Then, according to the work of Chang et al. [18], Kogut and Etsion [19] investigated the performance of sliding contact between a sphere and a plane. The fast Fourier transform (FFT) method was also introduced to investigate the problems of contact between the sphere and plane [20–22]. Zhou et al. [23,24] developed semi-analytic models with the FFT method to solve the problems of three-dimensional arbitrarily shaped inclusions in an isotropic half space. By breaking up the inhomogeneous inclusions into small cuboidal elements, Zhou et al. [25,26] also developed a general solution for multiple 3D arbitrarily-shaped inhomogeneous inclusions near surfaces under contact

\* Corresponding author.

E-mail address: [kzhou@ntu.edu.sg](mailto:kzhou@ntu.edu.sg) (K. Zhou).

loading. Based on the conjugate gradient technique, Polonsky [27] numerically investigated rough contact problems. Ghaednia et al. [28] proposed a new expression for the permanent deformation after the impact of a rod with a flat surface during both loading and unloading processes. Then, they studied the frictionless contact behavior of an elasto-plastic sphere with an elasto-plastic flat [29].

In order to investigate the friction contact which widely exists in dry contact [30,31], Brizmer et al. [32,33] investigated the influence of the stick on the elastic-plastic spherical contact. Zait et al. [34] investigated the influences of the stick on the unloading behaviors of the sphere contact between dissimilar materials. Mulvihill et al. [3] presented a sliding friction model for both cylindrical and spherical elastic-plastic contacting asperities. Based on the slip line theory, Jackson et al. [35] investigated the relationship between the average pressure and the yield strength in the case of a rigid sphere indenting a frictionless perfectly-plastic half-space. Zhou et al. [36–38] modeled line and point elasto-hydrodynamic lubrication contacts between a rigid body and a heterogeneous half-space with inclusions beneath its surface.

For many materials, the strain-hardening behavior is obvious during deformation. Olsson and Larsson [39] investigated the contact between elastic-plastic adhesive bodies obeying the power hardening law. Lan et al. [40] studied the influences of the elastic-plastic properties on the hardness of the material. Zhao et al. [41] developed an FE model for a frictionless sphere in contact with a power-law hardening elastic-plastic property. Then, Zhao et al. [42] investigated the loading and unloading performances of a power-law hardening spherical contact under stick contact condition. Considering frictional, oblique contact and strain hardening effects, Brake et al. [43] developed a new formulation for frictional elastic-plastic contact between two surfaces.

However, the above investigations have mostly focused on the initial performances of the asperity contact and neglected the performance degradation over time. In fact, the asperities on the contacting surfaces may experience repetitive interaction and suffer from fatigue damage, which can easily initiate a crack and significantly reduce the fatigue life of the components as well as the connection stiffness [44]. Recently, the failure of asperity has been studied by several scholars. Beheshti et al. [45] explained the wear mechanisms by asperity fatigue. Based on linear-elastic fracture mechanics, Xu [46] investigated the crack process of a two-dimensional asperity under normal contact. However, the studies on the fatigue damage-induced crack initiation and mechanical performance degradation of the asperity have been rarely reported.

Therefore, this work is concerned with the fatigue macro-crack initiation and the performance degradation of a cylindrical asperity in contact with a rigid flat under normal cyclic loadings. By coupling with the elastic-plastic constitutive model, a continuum damage mechanics (CDM)-based approach is introduced to derive the evolutions of stress, strain and damage of the material. The nonlinear kinematic hardening of the material is considered, and the damage evolution induced by both cyclic stress and accumulated plastic strain is calculated. The contact between a cylindrical asperity and a rigid flat under the normal cyclic loading is modeled. The macro-crack initiation and the evolutions of mechanical performances of the asperity, as well as their dependencies on the cyclic loadings, are discussed and presented.

## 2. Continuum damage mechanics (CDM) model

Fatigue damage can be considered as a progressive degradation of the material due to irreversible changes occurring in material microstructures. The initiation of macro-cracks will take place once the damage accumulates to a critical level. By coupling the mechanical behavior law and the CDM theory, a damage-coupled elastic-plastic constitutive model is developed to predict the damage and hardening behaviors of the material.

### 2.1. Damage-coupled elastic-plastic constitutive model

In the theory of CDM, a damage variable  $D$  is often introduced to estimate the deterioration of material caused by fatigue loadings. Fig. 1 illustrates a representative volume element (RVE) [47–50] to describe the damage of the material. The damage variable is a quantification of the surface density of micro-cracks, voids and cavities lying on an elemental cross-sectional plane. The mechanical measurement of the local damage relative to the direction  $\vec{n}$  is defined as

$$D_n = \frac{S_D}{S}, \quad (1)$$

where  $S$  denotes the total section area of RVE, and  $S_D$  the total damaged area. By assuming the isotropic damage evolution for the material, the damage tensor  $\mathbf{D}$  is reduced to a scalar defined as

$$D = \frac{S - S_R}{S}, \quad (2)$$

where  $S_R$  is the effective area of resistance, and can be expressed as  $S_R = S - S_D$ .

Over the total section of RVE, the total load  $P$  is resisted by the effective stress  $\tilde{\sigma}$  which can be identified as

$$\tilde{\sigma} = \frac{P}{S_R} = \frac{P}{(1-D)S} = \frac{\sigma}{1-D} = E\varepsilon^e, \quad (3)$$

where  $\varepsilon^e$  and  $\sigma$  are the strain and stress of the damaged material, respectively. Alternatively, the damaged material property can be expressed as

$$\sigma = E(1-D)\varepsilon^e = \tilde{E}\varepsilon^e, \quad (4)$$

where  $E$  and  $\tilde{E}$  are the elastic moduli of the initial and the damaged material, respectively. The Poisson's ratio remains unchanged in the damaged material [51]. The damage scalar can be rewritten as

$$D = 1 - \frac{\tilde{E}}{E}. \quad (5)$$

In engineering, damage measurement can be achieved by using the reduction of the elastic modulus.

The  $J_2$  flow model is employed in this study to simulate the elastic-plastic behavior. By combining the Mises yield criterion with the CDM theory, the Mises yield surface function  $F$  can be defined as

$$F = \sigma_{eq} - Q, \quad (6)$$

where  $\sigma_{eq}$  is the equivalent stress and defined as

$$\sigma_{eq} = \left[ \frac{3}{2} \left( \frac{\mathbf{S}}{1-D} - \boldsymbol{\alpha} \right) : \left( \frac{\mathbf{S}}{1-D} - \boldsymbol{\alpha} \right) \right]^{1/2}, \quad (7)$$

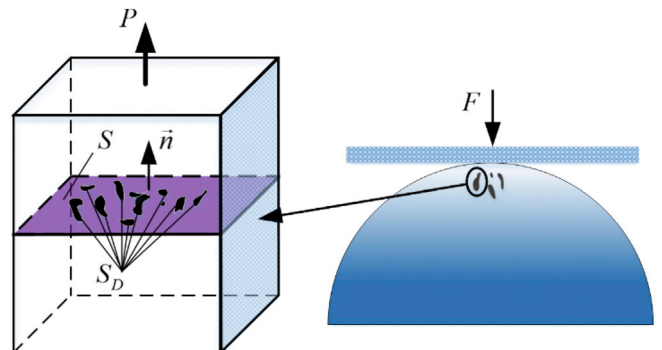


Fig. 1. Representative volume element.

where  $\mathbf{S}$  represents the deviatoric part of the Cauchy stress  $\sigma$ , and  $\boldsymbol{\alpha}$  is a back-stress tensor representing the center of the yield surface in the deviation space. The parameter  $Q$  is the radius of the yield surface with the evolution defined as

$$\dot{Q} = \dot{\lambda}b(Q_\infty - Q), \quad (8)$$

where the scalar  $\dot{\lambda}$  denotes the plastic flow rate. The material parameters  $b$  and  $Q_\infty$  should be determined experimentally.

In the condition of small strains, the total strain for the elastic-plastic deformation can be decomposed as

$$\boldsymbol{\varepsilon} = \boldsymbol{\varepsilon}^e + \boldsymbol{\varepsilon}^p, \quad (9)$$

where  $\boldsymbol{\varepsilon}^e$  and  $\boldsymbol{\varepsilon}^p$  are the elastic and plastic strains, respectively.

The stress tensor can be calculated as [52].

$$\boldsymbol{\sigma} = (1 - D)\mathbf{C} : \boldsymbol{\varepsilon}^e = (1 - D)\mathbf{C} : (\boldsymbol{\varepsilon} - \boldsymbol{\varepsilon}^p), \quad (10)$$

where  $\mathbf{C}$  is the fourth-order elastic tensor. The presence of damage corresponds to the reduction of the elastic modulus.

A rate-independent plasticity model is adopted, and the plastic strain rate can be expressed as [52].

$$\dot{\boldsymbol{\varepsilon}}^p = \dot{\lambda} \frac{\partial F}{\partial \boldsymbol{\sigma}} = \dot{\lambda} \frac{3}{2} \frac{\frac{\mathbf{S}}{1-D} - \boldsymbol{\alpha}}{\sigma_{eq}(1-D)}, \quad (11)$$

where  $\partial F / \partial \boldsymbol{\sigma}$  represents the plastic flow direction.

The accumulated plastic strain rate  $\dot{p}$  can be determined as

$$\dot{p} = \sqrt{\frac{3}{2} \dot{\boldsymbol{\varepsilon}}^p : \dot{\boldsymbol{\varepsilon}}^p} = \frac{\dot{\lambda}}{1-D}. \quad (12)$$

By combing Eqs. (11) and (12), the equation of the plastic strain rate can be derived from

$$\dot{\boldsymbol{\varepsilon}}^p = \frac{3}{2} \dot{p} \frac{\frac{\mathbf{S}}{1-D} - \boldsymbol{\alpha}}{\sigma_{eq}}. \quad (13)$$

In order to estimate the yield surface movement induced by kinematic hardening, the nonlinear kinematic hardening model (AF-NLKH model) proposed by Armstrong and Frederick [53–55] is introduced to divide  $\boldsymbol{\alpha}$  into several components as

$$\boldsymbol{\alpha} = \sum_{k=1}^M \boldsymbol{\alpha}^{(k)}, \quad (14)$$

and

$$\dot{\boldsymbol{\alpha}}^{(k)} = (1 - D) \left( \frac{2}{3} C_k \dot{\boldsymbol{\varepsilon}}^p - \gamma_k \boldsymbol{\alpha}^{(k)} \dot{p}^{(k)} \right), \quad (15)$$

where  $M$  denotes the number of the back-stress components. The material parameters  $C_k$  and  $\gamma_k$  should also be determined from the stress-strain curve obtained from uniaxial tensile testing.

## 2.2. Damage evolution models

Under cyclic loadings, the contact between an asperity and a rigid plane may produce both elastic and plastic deformations, which may induce fatigue damage and change the contact response [56,57]. In this study, both the elastic damage model induced by the cyclic stresses and the plastic damage model induced by accumulated plastic strains are employed [52].

### 2.2.1. The elastic damage evolution model

The elastic damage evolution model can be expressed as [48,58–60].

$$\frac{dD^e}{dN} = \left[ 1 - (1 - D)^{\beta+1} \right]^\eta \left[ \frac{A_{II}}{M_0(1 - 3b_2\sigma_{H,\text{mean}})(1 - D)} \right]^\beta, \quad (16)$$

Where  $N$  is the cyclic number;  $A_{II}$  is the octahedral shear stress amplitude during a total loading cycle, and can be obtained by

$$A_{II} = \frac{1}{2} \left[ \frac{3}{2} (S_{ij,\text{max}} - S_{ij,\text{min}}) (S_{ij,\text{max}} - S_{ij,\text{min}}) \right]^\frac{1}{2}, \quad (17)$$

where  $S_{ij,\text{min}}$  and  $S_{ij,\text{max}}$  are the minimum and maximum deviatoric stresses in one cycle, respectively.

The mean hydrostatic stress  $\sigma_{H,\text{mean}}$  in one cycle is defined as

$$\sigma_{H,\text{mean}} = \frac{1}{6} (\sigma_{H,\text{max}} + \sigma_{H,\text{min}}), \quad (18)$$

where  $\sigma_H$  is the hydrostatic stress, of which the maximum and minimum values in one cycle are represented by  $\sigma_{H,\text{max}}$  and  $\sigma_{H,\text{min}}$ , respectively. In Eq. (16), the parameter  $\eta$  with the Sines fatigue limit criterion [50,56,60] is given by

$$\eta = 1 - a \left( \frac{A_{II} - A_{II}^*}{\sigma_u - \sigma_{eq,\text{max}}} \right), \quad (19)$$

and

$$A_{II}^* = \sigma_{t0}(1 - 3b_1\sigma_{H,\text{mean}}), \quad (20)$$

Where  $\langle \bullet \rangle$  means that  $\langle x \rangle = 0$  as  $x \leq 0$  and  $\langle x \rangle = x$  as  $x > 0$ . The parameter  $\sigma_{eq,\text{max}}$  is the maximum equivalent stress in one cycle.

By integrating Eq. (16) from  $D = 0$  to  $D = 1$  for uniaxial fatigue, the number of cycles to failure under an assumed constant loading can be expressed as

$$N_f = \frac{1}{1 + \beta} \frac{1}{aM_0^{-\beta}} \frac{\langle \sigma_u - \sigma_{\text{max}} \rangle}{\langle \sigma_u - \sigma_{t0}(1 - b_1\bar{\sigma}) \rangle} \left[ \frac{\sigma_u}{1 - b_2\bar{\sigma}} \right]^{-\beta}, \quad (21)$$

where  $\sigma_{\text{max}}$  denotes the maximum stress,  $\sigma_u$  the stress amplitude and  $\bar{\sigma}$  the mean stress in the uniaxial fatigue case. The ultimate tensile stress  $\sigma_u$  can be derived from the monotonic tensile strain-stress curve. The parameters  $b_1$  and  $b_2$  can be derived from fatigue testing with different mean stresses;  $\sigma_{t0}$ ,  $\beta$  and  $aM_0^{-\beta}$  can be obtained from fatigue test which is stress-controlled in the condition of a fully reversed loading. The parameter  $a$  is measured through modulus degradation during fatigue tests [48,56,60].

### 2.2.2. The plastic damage accumulation model

Based on the accumulated plastic strain, the plastic damage model can be expressed as [52,61,62].

$$\frac{dD^p}{dN} = \left[ \frac{(\sigma_{\text{max}}^*)^2}{2ES(1 - D)^2} \right]^m \dot{p}, \quad (22)$$

where  $\sigma_{\text{max}}^*$  represents the maximum damage equivalent stress in one cycle [61]. The damage equivalent stress is given by

$$\sigma^* = \sigma_{eq} R_v^\frac{1}{2}, \quad (23)$$

where the triaxiality function of stress  $R_v$  can be obtained by

$$R_v = \frac{2}{3} (1 + \nu) + 3(1 - 2\nu) \left( \frac{\sigma_H}{\sigma_{eq}} \right)^2. \quad (24)$$

Through a strain-controlled low-cycle fatigue test, the parameters  $S$  and  $m$  can be determined. As the Coffin-Manson law puts forward, the strain-life curve can be portrayed as [47,49].

$$\frac{\Delta \varepsilon_p}{2} = \varepsilon_f (2N_f)^c, \quad (25)$$

where  $\varepsilon_f$  and  $c$  are fatigue ductility coefficients obtained from fatigue testing.

The cyclic stress-strain curve is expressed as

$$\sigma_{\max} = K' \left( \frac{\Delta \varepsilon_p}{2} \right)^{n'}, \quad (26)$$

where  $K'$  and  $n'$  are the material parameters.

By integrating the plastic damage model from  $D = 0$  to 1, the number of cycles that lead to failure for a uniaxial loading case can be expressed as

$$N_f = \frac{1}{2(2m+1)} \left( \frac{2^{1+2n'} ES}{(K')^2} \right)^m (\Delta \varepsilon_p)^{-(1+2mn')}. \quad (27)$$

After obtaining  $\varepsilon_f$ ,  $c$ ,  $K'$  and  $n'$  from fatigue testing [61], the parameters  $S$  and  $m$  can also be determined from Eqs. (25) and (27).

### 3. Numerical scheme for solving the damage evolution

In metals, the initiation of fatigue macro-cracking is mainly caused by accumulations of micro-cracks and cavities [2]. The macro-crack can occur easily in a damage zone, and the macro-crack initiation can be simulated based on the currently available damage prediction models [45,63].

#### 3.1. FEM model of cylindrical asperity contact

In this study, an asperity in cylindrical contact with a rigid plane under cyclic loadings is modeled and analyzed. The FE software ABAQUS 6.14 is used throughout the modeling work. The proposed damage-coupled elastic-plastic constitutive model is implemented by the “ABAQUS/Explicit” scheme with the user subroutine VUMAT.

Initially, it is intended to conduct the simulation using the implicit solver “ABAQUS/Standard” with the user subroutine UMAT, which provides quasi-static results. However, the implicit solver will encounter convergence difficulties when large compression is modeled [3]. The explicit solver “ABAQUS/Explicit” can also be well implemented to solve quasi-static problems [3] and be more robust in handling contact problems and thus damage predictions. Therefore, the explicit solver “ABAQUS/Explicit” with VUMAT is adopted.

In many cases, the mechanical components interact with counterparts in line contact [64]. For line contact problems, a cylinder body in contact with a rigid plane is commonly adopted. In this study, by treating the normal cylindrical contact as a plane-strain problem, a cylindrical contact

problem is investigated so that a model could be developed in “ABAQUS/Explicit” with reasonable computation time.

The schematic and the FE model of a cylindrical asperity in contact with a rigid plane are shown in Fig. 2 (a). The asperity is modeled as a deformable instance and the plane is modeled as rigid. Due to the scale-independence of the continuum mechanics model [3], a generic cylindrical asperity with the radius of  $R = 20$  mm and thickness of  $T = 0.4$  mm is chosen. Given the symmetry in the normal contact case, only half of the cylinder is modeled. The subsurface stresses under the contact region distribute complexly and have high values, which requires a finer mesh in this region. In order to reduce the computation cost, the meshes become gradually more and more coarse as they move away from the contact region. The size ratio of the smallest element to the largest one is about 2.4%.

The deformation of the body is enforced by the displacement acting on the rigid plane in two steps as shown in Fig. 2 (b). The first step lasts for 0.5 s, and the initial displacement with the value of  $A_i$  is exerted on the plane gradually to establish the contact between the cylinder and the plane. In the second step, based on the “Periodic Amplitude” function in ABAQUS, a sinusoidal oscillation with the amplitude of  $A_o$  and the period of 2 s is applied to the plane. This oscillation will last until the macro-crack nucleates.

By constraining the normal movement of both front and back planar faces (i.e.  $u_z = 0$ ,  $u'_x = u'_y = 0$ ), the cylindrical body degrades into a plane strain slice. The base of the body is fixed with “Encastre constraint”. The rigid plane is enforced with displacement-load which is in the form of sinusoid with an initial amplitude  $A_i$  and a oscillation amplitude of  $A_o$ . In this study, only the normal load is considered. To secure a higher accuracy and better stability, the “General contact algorithm” together with the “penalty friction formulation” assuming friction coefficient to be 0.1 is utilized for the explicit analysis.

Since “Abaqus/Explicit” is a dynamic analysis program and the static contact is expected in this study, the rigid plane must be loaded slowly enough to eliminate inertia effect. However, the very slow loading rate can ensure quasi-static solutions but it is computationally expensive. The computation time required for this analysis can be reduced in either one of the two equivalent ways: the loading rate can be increased incrementally until any further increase in loading rate would no longer result in a quasi-static solution, or mass scaling can be used [65]. In this study, the “Mass scaling” is adopted to ensure the quasi-static modeling and reduce the analysis cost. The quasi-static results can be assumed if the kinetic energy from the model only counts for a minor percent of the internal strain energy [3].

#### 3.2. Numerical implementation

The simulation of the damage accumulation for the whole fatigue lifetime is computationally expensive. In order to speed up the

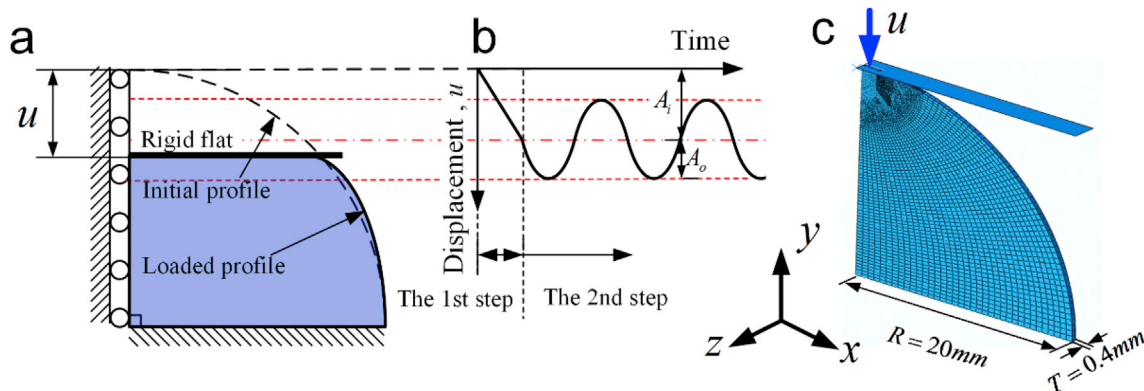


Fig. 2. The schematic and the FE model of a cylindrical body in contact with a flat: (a) the geometry and loading conditions; (b) steps and displacement history; and (c) the Finite element model.

simulation, a jump-in-cycles procedure is introduced by assuming the stress, accumulated plastic strain and damage unchanged over a finite number of  $\Delta N$  cycles. Here,  $\Delta N$  can be considered as a speed up factor, and constitute a block. The above algorithm can be interpreted as follows:

- (1) The initial contact between the asperity and rigid plane is modeled, and the damage of the whole model is initialized to be zero.
- (2) Based on the damage-coupled elastic-plastic constitutive model, the contact is solved for the plastic strain, elastic strain, and stress. At the beginning of each time increment, the VUMAT is called by all of the integral points of the model to update solution-dependent state variables and stress. The histories of accumulated plastic strain and stress, in the current block  $i$ , are calculated and saved.
- (3) According to the stress and accumulated plastic strain, the damage increase rate in the current block is calculated based on the damage evolution models, as

$$\left(\frac{dD}{dN}\right)_j^i = \left(\frac{dD^e}{dN}\right)_j^i + \left(\frac{dD^p}{dN}\right)_j^i, \quad (28)$$

where superscript  $i$  denotes the current block, and  $j$  the number of the element. It is noticeable that the plastic damage increase will vanish if no plastic deformation occurs as done in Refs. [56,57,66].

- (4) Once the damage evolution rate of every integral point is obtained in the current block, the maximum is chosen and saved as

$$\left(\frac{dD}{dN}\right)_{\max}^i = \max\left(\left(\frac{dD}{dN}\right)_j^i\right). \quad (29)$$

- (5) The jump-in-cycles procedure requires only one speed up factor  $\Delta N^i$  utilized for the whole model. A critical damage increase  $\Delta D_c$  is determined ahead to limit the increment of damage in a block. Thus,

$$\Delta N^i = \text{int}\left(\frac{\Delta D_c}{\left(\frac{dD}{dN}\right)_{\max}^i}\right). \quad (30)$$

- (6) At the end of the current block, the damage and the number of cycles for the whole model are accumulated as

$$D_j^{i+1} = D_j^i + \left(\frac{dD}{dN}\right)_j^i \Delta N^i, \quad (31)$$

and

$$N^{i+1} = N^i + \Delta N^i. \quad (32)$$

- (7) The material properties of the integral point are updated to reflect the material degradation as

$$\begin{cases} E_j^{i+1} = E(1 - D_j^{i+1}) \\ (C_k)_j^{i+1} = C_k(1 - D_j^{i+1}) \\ (\gamma_k)_j^{i+1} = \gamma_k(1 - D_j^{i+1}) \\ (\sigma_y)_j^{i+1} = \sigma_y(1 - D_j^{i+1}) \end{cases}. \quad (33)$$

- (8) Steps (2)–(7) are repeated until the critical damage value  $D_c$  is reached on one of the integral points in the model. In the present work, the size of the element in the damage zone is about  $50\mu\text{m}$ , which is about the same size as the initial macro-crack [67]. Therefore, the occurrence of an element with the damage value of  $D_c$  can be considered as the nucleation of the macro-crack from an engineering view of point.

#### 4. Results and discussion

In this study, Ti-6Al-4V is adopted to model the asperity. Its material parameters of the elastic-plastic constitutive model are determined from uniaxial monotonic tension test [56] and listed in Table 1. It is assumed that the material is initially virgin, i.e.,  $D_0 = 0$ . The isotropic hardening effect of the material is neglected, but the kinematic hardening is considered. Zhang et al. [56] conducted fatigue tests with standard specimens of Ti-6Al-4V to determine the material damage constants in both the elastic and plastic damage models as listed in Table 2.

Based on the material constitutive parameters listed in Table 1, Fig. 3 shows the stress-strain relationship in both loading and unloading processes, which is calculated in “ABAQUS/Explicit” with user subroutines VUMAT through performing on the FE model with a single element. By comparing with the experiment data obtained from a unidirectional loading test, it can be found that the constitutive model established in the VUMAT can well reflect the material tensile constitutive properties.

##### 4.1. The evolutions of damage and mechanical performances of the asperity

The oscillation of the rigid flat will induce fatigue damage of the asperity. In order to express the load amplitudes used in the following simulations, both the critical penetration  $\omega_c$  and the corresponding critical normal contact force  $P_c$  are introduced. The critical penetration indicates the first occurrence of the plastic yielding in a quasi-static normal contact between a cylinder and a rigid plane [68]. The simulation for the case with the initial compression of  $A_i = 5\omega_c$  and the oscillation amplitude of  $A_o = A_i/4$  is first conducted to reveal some performances of the connecting asperities.

In this study, the nucleation location and moment of the macro-crack are chosen as the damage variables to judge whether the mesh size and  $\Delta D_c$  are convergent. In order to obtain the convergent model, the mesh density and  $\Delta D_c$  are doubled iteratively until appropriate convergences of damage variables are achieved. A difference of 1% between two consecutive attempts is used as the convergence criterion for the nucleation location of the macro-crack. In the case with high cyclic load ( $A_i = 6\omega_c$  and  $A_i = 7\omega_c$ ), a convergence criterion of 1% is used for the nucleation moment of the macro-crack. While in the case with the low cyclic load ( $A_i = 4\omega_c$  and  $A_i = 5\omega_c$ ), a convergence criterion of 0.5% is adopted. In the subsequent simulations, a mesh (see Fig. 2 (c)) with a total of 16,333 linear hexahedral elements (C3D8) is chosen. A critical damage increase  $\Delta D_c = 0.01$  is utilized in the jump-in-cycles procedure. This critical damage increase has proved its efficiency and accuracy in the following calculation. In order to ensure the explicit analysis a quasi-static process, the kinematic energy during the analysis should be a small fraction of the internal strain energy (<10% according to [69]). The mass scaling factor with a value of  $1E6$  can ensure the quasi-static process.

Fig. 4 shows the evolution of damage distribution until the macro-crack initiation. The damage varies from cycle to cycle, and mainly concentrates in a very small zone relative to the whole model. During the first cycle, the damage is derived mainly from plastic deformation and

**Table 1**  
Material constitutive parameters for Ti-6Al-4V [56].

$E$ (MPa)	$\nu$	$\sigma_y$ (MPa)	$C_1$ (MPa)	$C_2$ (MPa)	$\gamma_1$	$\gamma_2$
116,000	0.34	965	136,500	8100	1050	45

**Table 2**  
Damage parameters for Ti-6Al-4V [56].

$S$	$m$	$\sigma_u$ (MPa)	$\sigma_{l0}$ (MPa)	$\beta$	$M_0$	$b_1$	$b_2$	$a$
9.9293	4.7846	1180	358	2.1	1.1434E5	1.30E-3	5.50E-4	0.75

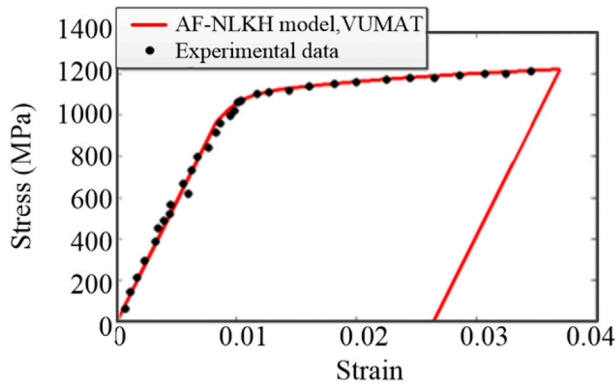


Fig. 3. The stress-strain curve for Ti-6Al-4V.

highly localized in the subsurface near to the contact point. In the following cycles, the damage softens the material, which makes the plastic deformation and damage easier. As the cycles increase up to 304, the zone subject to high damage nearly shrinks to the most critical element 9954, and the maximum damage accumulates to the critical value of  $D_c$ , which means that the macro-crack nucleates at this moment.

Fig. 5 presents the evolution and increase rate of damage for the element 9954 from  $D = D_0$  to  $D = D_c$ . In the first cycle, a large plastic deformation occurs and an obvious damage increase is induced (Fig. 5 b). Without the consideration of the damage, plastic deformation will not happen anymore after the first cycle under the current cyclic loading with constant amplitude. However, in the real case, the damage will accumulate and soften the material. At the beginning of the cyclic loading, only a small damage emerges in a concentrated zone, which will slightly decrease the material properties and induce a tiny damage increment during the following cycles. However, with the increase of cycles, the softening effect of damage on the material becomes more and more obvious due to the gradually accumulated damage, which in turn further degrades the material with an increasing damage rate. After about 304 cycles, the damage of element 9954 increases with a high rate, and reaches the critical value  $D_c$  rapidly.

The progressive evolution of damage will soften the material and thus result in the redistribution of the stress. Fig. 6 lays out the Mises stress distributions at the ends of the first and 304th loading processes. It can be found that the redistribution is obvious in the area where damage occurs. Under cyclic loading with constant amplitude, the damage reduces the stress due to the softening effect. Fig. 7a presents the evolution of the

maximum equivalent stress ( $\sigma_{e,max}$ ) distributed along y axle. It can be found that the damage mainly affects the stress distribution in the area under the contact region, especially on the critical element 9954.

Fig. 7b shows the evolution of  $\sigma_{e,max}$  of the element 9954. It can be found that the maximum stress occurs under the contact zone as observed in Refs. [64,70]. The evolution of the  $\sigma_{e,max}$  has the same tendency with that of the damage (Fig. 5a). Due to the softening effect of the damage, the decrease of the equivalent stress on the element 9954 becomes increasingly obvious. Until the macro-crack initiates, the  $\sigma_{e,max}$  has decreased from 1098 to 814 MPa.

As stated in Eq. (22), the equivalent plastic strain (PEEQ) has a direct relationship with the plastic damage. The PEEQ of the model shown in Fig. 8 also presents a similar distribution and evolution with those of damage, which can be concluded that in the current case, the damage is mainly derived from the plastic deformation. In fact, the plastic strain and damage interact as both cause and effect. The plastic strain will cause damage of the material, while the damage will in turn degrade the properties of the material and cause the plastic deformation in the subsequent cycles.

Fig. 9 presents the evolution of PEEQ on the element 9954. It can be found that the PEEQ has the same increase tendency with that of the damage until the macro-crack initiates (Fig. 5 a). During the 1st and the 304th cycles, PEEQ has a large increase, which gives rise to a large damage increase. The plastic strain in the first cycle is mainly caused by the large deformation of the virgin material without kinematic hardening, while the plastic strain in the 304th cycles mainly results from the softening effect of the accumulated damage.

Fig. 10a presents the evolution of the stress-strain relationship in y direction at the first integral point of the element 9954 under the cyclic loading with  $A_i = 5\omega_c$  and  $A_o = A_i/4$ , and Fig. 10b shows the evolution for the first five blocks in detail. It is obvious that due to the softening effect of damage, the maximum stress and the elastic modulus in each block decline as the cycle increases. The plastic strain occurring in the first cycle is much larger than that in the following cycles, which can also be found in Fig. 9 b. This is because that in the first cycle, the initial material experiences both the elastic and plastic deformations. The elastic strain is recoverable, but the plastic strain is irreversible. From the second cycle, if the damage is not considered, no plastic strain will occur again at all, and only the elastic strain exists.

However, the damage induced by both the elastic and plastic deformations in the last cycle will soften the material and thus reduce the elastic modulus, which will cause tiny plastic and increase of the elastic strain. Therefore, it can be considered that the subsequence plastic strain is mainly caused by the damage. In this process, both the damage as well

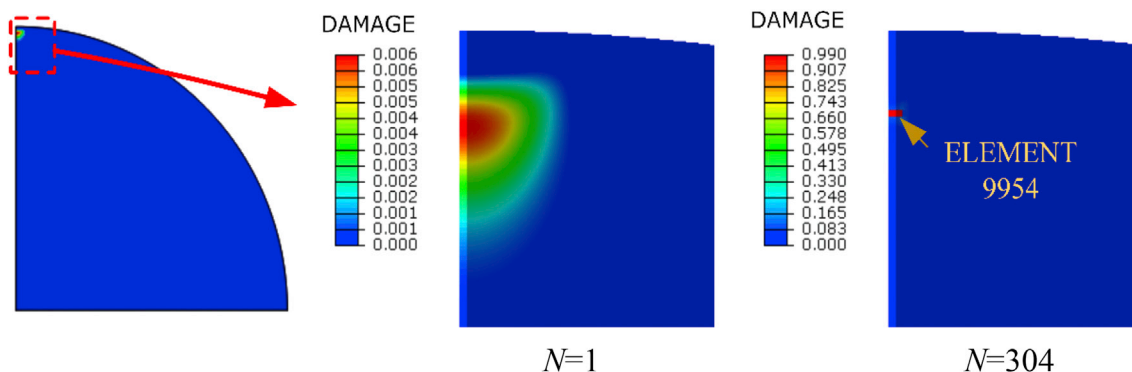


Fig. 4. The evolution of damage distribution in the case with  $A_i = 5\omega_c$  and  $A_o = A_i/4$ .

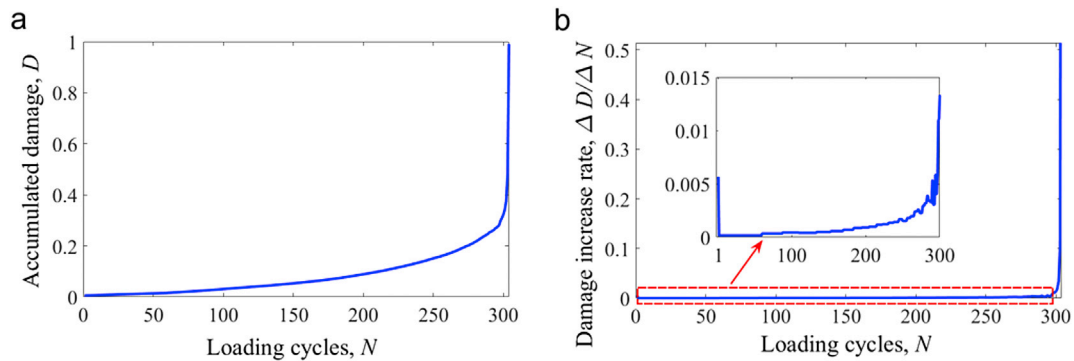


Fig. 5. The evolution of damage on the element 9954: (a) the accumulated damage, and (b) the increase rate of damage.

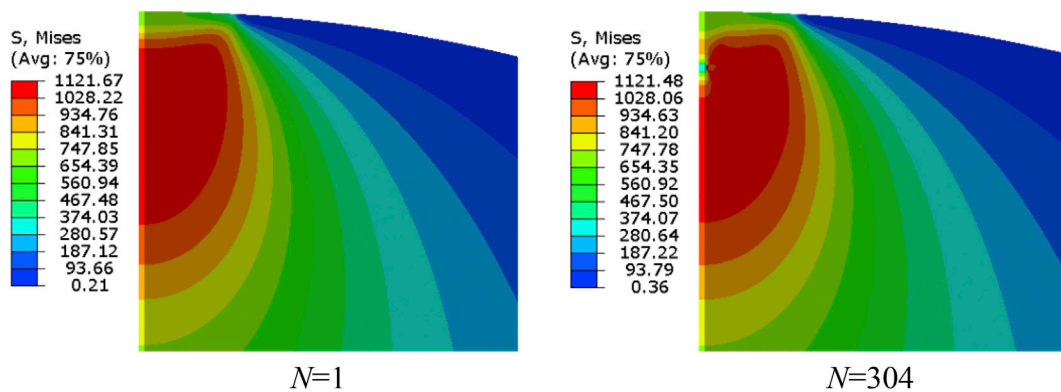


Fig. 6. The change of the Mises stress distribution.

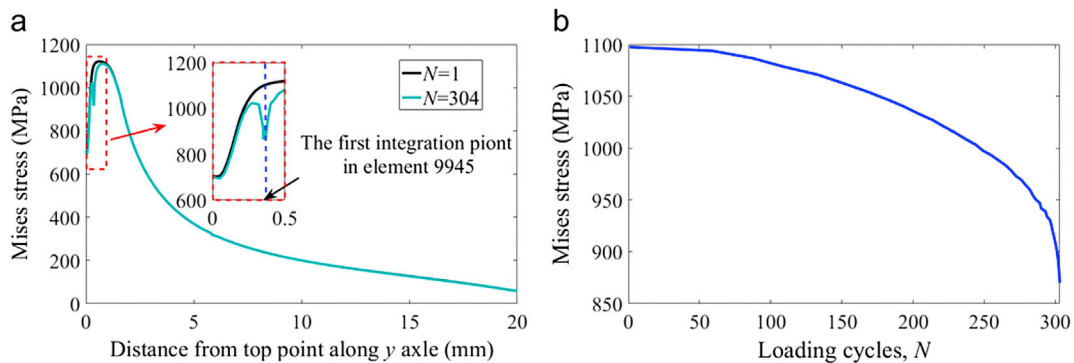


Fig. 7. The evolution of the maximum equivalent stress (a) distributed along y axle, and (b) on the element 9954.

as the reduction of the elasticity modulus are very small, and thus the plastic strain and the increase of the elastic strain are not obvious. Therefore, the subsequent strain is smaller than that in the first cycle. As it comes to the 304th cycle, the accumulated damage is considerable, which in turn accelerates the damage accumulation and thus nucleates macro-crack as shown in Fig. 5. At this moment, the damage is big enough to obviously soften the material and produce large elastic and plastic strains.

The softening effect of fatigue damage will decrease the reaction forces between the asperity and the rigid plane. Fig. 11 presents the evolution of the mean reaction forces in each cycle until the macro-crack nucleates. The forces are normalized with the critical normal contact force  $P_c$ . It is obvious that with the increase of cycles, the capacity for the asperity to support the plane reduces. The reason is that the damage is expedited and extended with the increase of time (Fig. 4).

#### 4.2. The influences of cyclic loadings on fatigue lifetime and mechanical performances

Subsequently, the influences of different cyclic loadings on the damage-induced crack initiation lifetime, as well as the evolution of mechanical performances of the asperity, are also investigated. The loadings with initial penetrations varying from  $A_i = 4\omega_c$  to  $A_i = 7\omega_c$ , and two oscillation displacements with the amplitude of  $A_o = A_i/2$  and  $A_o = A_i/4$  in each case, are modeled and analyzed.

Fig. 12 lays out the comparison of crack initiation lifetime under different cyclic loadings. It is clear that with the increase of the initial penetration, the lifetime of the asperity will decline dramatically. Furthermore, such tendency will be pronounced when the rigid plane oscillates with larger displacement amplitudes. The reason is that the initial penetration determines the average deformation in a cycle, and the

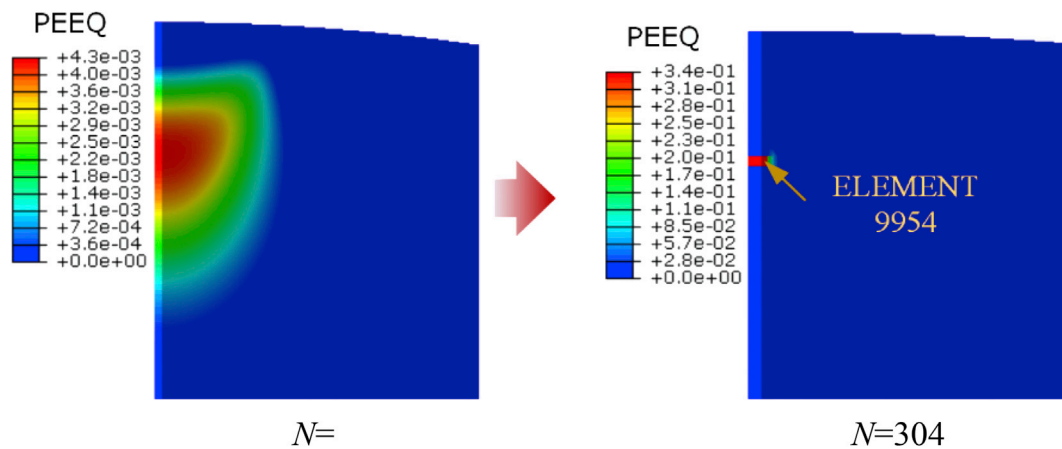


Fig. 8. The evolution of the accumulated equivalent plastic strain.

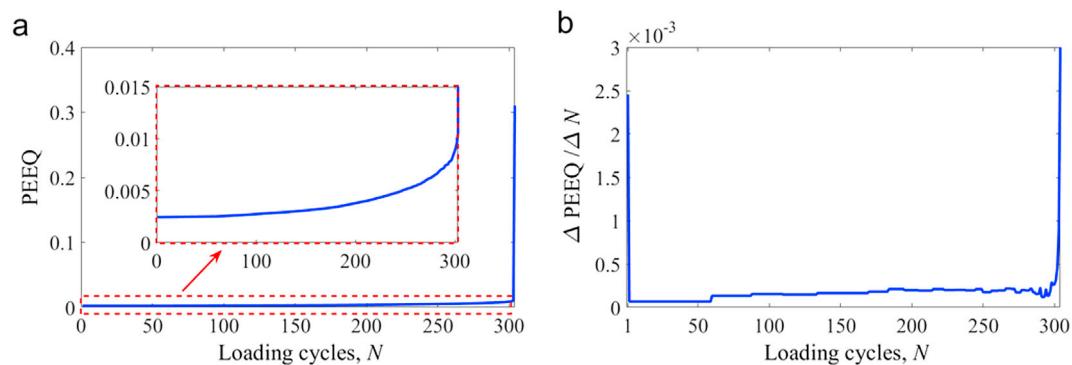


Fig. 9. The evolution of the accumulated plastic strain of element 9954.

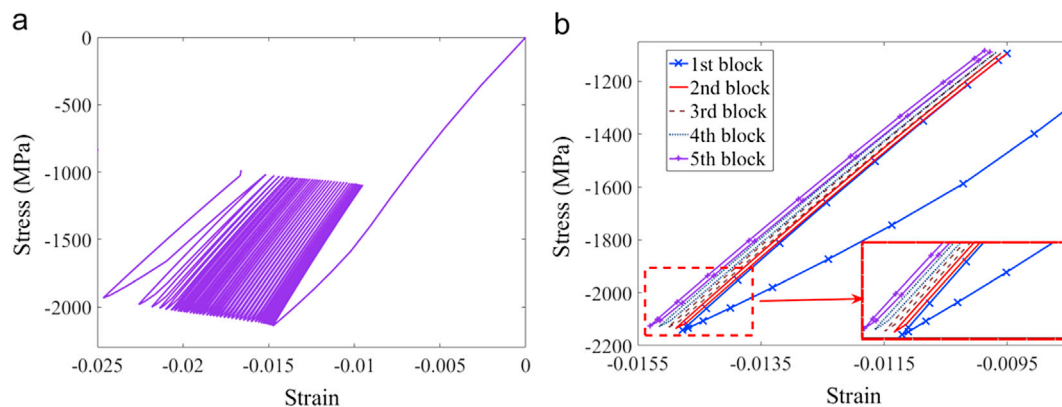


Fig. 10. The evolution of Stress-strain relationship for the element 9954: (a) all of the blocks, and (b) the first five blocks.

higher deformation will give rise to more plasticity damage. In addition, the larger oscillation penetration means the larger stress and strain during the loading phase, which will accumulate damage and thus shorten the lifetime.

The damage will soften the material, and thus reduce the reaction force between the asperity and rigid plane. Table 3 compares the changes of reaction forces for all of the investigated cases. It can be found that with the increase of the penetration, not only the lifetime but also reaction forces will be obviously reduced, and the larger displacement oscillation can pronounce this reduction.

In addition, fatigue failure process is constituted by crack initiation and propagation, with the former dominating the fretting fatigue lifetime [2]. Before the crack nucleation, the reduction of the reaction force is not

obvious. However, the crack propagation after the nucleation will quickly cause surface asperities fracture and formation of abrasive, which will result in the fatigue failure and thus dramatically decrease properties of the contacting rough surfaces.

## 5. Conclusion

This study establishes a damage-coupled elastic-plastic constitutive model in the purpose of predicting the damage accumulation in the material subject to cyclic loadings. The elastic-plastic behavior of the material with kinematic hardening effects is taken into consideration. Regarding the damage evolution, it relies on the calculation of the cyclic stress-based elastic damage model and the plastic strain-based plastic

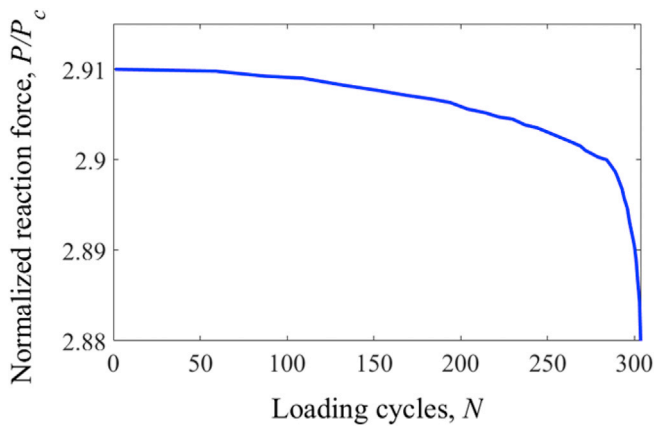


Fig. 11. The evolution of the reaction forces acting on the rigid plane.

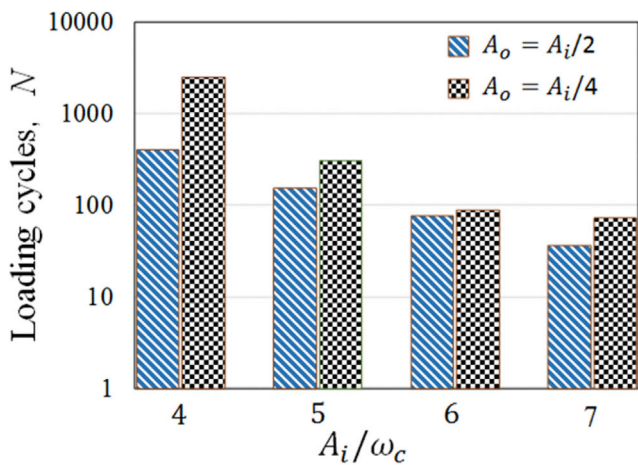


Fig. 12. The comparisons of the fatigue crack initiation lifetimes for different cases.

**Table 3**  
The comparisons of the evolution of reaction forces under different cyclic loadings.

$A_i/\omega_c$	$A_o/A_i$	Average reaction forces, $P/P_c$		Reduction, %
		Initial	Final	
4	1/2	2.25	2.22	1.12
	1/4	2.30	2.28	0.899
5	1/2	2.79	2.74	1.66
	1/4	2.91	2.88	1.10
6	1/2	3.28	3.21	2.17
	1/4	3.50	3.46	1.25
7	1/2	3.73	3.65	2.21
	1/4	4.06	3.98	2.02

damage model. The model put forward is carried out through “ABAQUS/Explicit” with the user subroutine VUMAT.

A contact model of an asperity in cylindrical contact with a rigid flat subject to normal cyclic loadings is established. Both the fatigue crack initiation and the degradation of mechanical properties of the asperity are investigated. The damage is accumulated from cycle to cycle and intensively localized in the subsurface near the contact point. After finite cycles, the damage concentrates in a small zone and nucleates a macro-crack, which reduces the capacity for the asperity to support the plane. With increasing initial penetration and oscillation between rigid plane and asperity, the damage will be expedited and the lifetime of asperity will be further shortened.

This investigation only conducts a cylindrical contact simulation. In

the future work, the investigations on the damage of the spherical contact under both sliding and suppress loads will be furthered. Moreover, the current approach focusing on a single asperity will be extended to a 3D rough contacting surface.

**Acknowledgments**

Bo Zhao is grateful to the China Postdoctoral Science Foundation (2015M57036). Kun Zhou acknowledges the Ministry of Education - Singapore (Academic Research Fund TIER 1 RG174/15).

**References**

- [1] Ren Y, Beards C. Identification of effective linear joints using coupling and joint identification techniques. *J Vib Acoust* 1998;120:331–8.
- [2] Hojjati-Talemi R, Wahab MA, De Pauw J, De Baets P. Prediction of fretting fatigue crack initiation and propagation lifetime for cylindrical contact configuration. *Tribol Int* 2014;76:73–91.
- [3] Mulvihill D, Kartal M, Nowell D, Hills D. An elastic–plastic asperity interaction model for sliding friction. *Tribol Int* 2011;44:1679–94.
- [4] Goltsberg R, Etsion I. A universal model for the load–displacement relation in an elastic coated spherical contact. *Wear* 2015;322:126–32.
- [5] Johnson KL, Johnson KL. *Contact mechanics*. Cambridge university press; 1987.
- [6] Greenwood JA, Williamson JBP. Contact of nominally flat surfaces. *Proc R Soc Lond Ser A Math Phys Sci* 1966;295:300–19.
- [7] Bogy D. An elastic–plastic model for the contact of rough surfaces. *J Tribol* 1987; 109:257.
- [8] Maietta DM, Chang L. An asperity microcontact model incorporating the transition from elastic deformation to fully plastic flow. 2000.
- [9] Kogut L, Etsion I. Elastic–plastic contact analysis of a sphere and a rigid flat. *J Appl Mech* 2002;69:657–62.
- [10] Jackson RL, Green I. A finite element study of elasto–plastic hemispherical contact against a rigid flat. *J Tribol* 2005;127:343–54.
- [11] Shankar S, Mayuram MM. Effect of strain hardening in elastic–plastic transition behavior in a hemisphere in contact with a rigid flat. *Int J Solids Struct* 2008;45: 3009–20.
- [12] Olsson E, Larsson PL. A unified model for the contact behaviour between equal and dissimilar elastic–plastic spherical bodies. *Int J Solids Struct* 2016;81:23–32.
- [13] Shankar S, Arjun K. Effect of strain hardening during unloading for an elastic–plastic hemisphere in contact with a rigid flat. *Mech Adv Mater Struct* 2014;21:139–44.
- [14] Kadin Y, Kligerman Y, Etsion I. Unloading an elastic–plastic contact of rough surfaces. *J Mech Phys Solids* 2006;54:2652–74.
- [15] Brake MR. An analytical elastic–perfectly plastic contact model. *Int J Solids Struct* 2012;49:3129–41.
- [16] Etsion I, Kligerman Y, Kadin Y. Unloading of an elastic–plastic loaded spherical contact. *Int J Solids Struct* 2005;42:3716–29.
- [17] Kadin Y, Kligerman Y, Etsion I. Loading–unloading of an elastic–plastic adhesive spherical microcontact. *J Colloid Interface Sci* 2008;321:242–50.
- [18] Chang W-R, Etsion I, Bogy D. Static friction coefficient model for metallic rough surfaces. *J Tribol* 1988;110:57–63.
- [19] Kogut L, Etsion I. A semi-analytical solution for the sliding inception of a spherical contact. *J Tribol* 2003;125:499–506.
- [20] Liu S, Wang Q, Liu G. A versatile method of discrete convolution and FFT (DC-FFT) for contact analyses. *Wear* 2000;243:101–11.
- [21] Chen WW, Wang QJ. A numerical static friction model for spherical contacts of rough surfaces, influence of load, material. *Rough J Tribol* 2009;131:021402.
- [22] Wang Z-J, Wang W-Z, Wang H, Zhu D, Hu Y-Z. Partial slip contact analysis on three-dimensional elastic layered half space. *J Tribol* 2010;132:021403.
- [23] Zhou K, Chen WW, Keer LM, Wang QJ. A fast method for solving three-dimensional arbitrarily shaped inclusions in a half space. *Comput Methods Appl Mech Eng* 2009; 198:885–92.
- [24] Zhou K. Elastic field and effective moduli of periodic composites with arbitrary inhomogeneity distribution. *Acta Mech* 2012;223:293–308.
- [25] Zhou K, Keer LM, Wang QJ, Shah BM, Su F. Modelling damage to real surfaces in contact within a unified framework. *Procedia Eng* 2011;10:1573–8.
- [26] Zhou K, Keer LM, Jane Wang Q, Ai X, Sawamiphakdi K, Glaws P, et al. Interaction of multiple inhomogeneous inclusions beneath a surface. *Comput Methods Appl Mech Eng* 2012;217–220:25–33.
- [27] Polonsky IA, Keer LM. A numerical method for solving rough contact problems based on the multi-level multi-summation and conjugate gradient techniques. *Wear* 1999;231:206–19.
- [28] Ghaednia H, Marghitu DB, Jackson RL. Predicting the permanent deformation after the impact of a rod with a flat surface. *J Tribol* 2015;137:011403.
- [29] Ghaednia H, Pope SA, Jackson RL, Marghitu DB. A comprehensive study of the elasto–plastic contact of a sphere and a flat. *Tribol Int* 2016;93:78–90.
- [30] McGuiggan PM. Stick slip contact mechanics between dissimilar materials: effect of charging and large friction. *Langmuir* 2008;24:3970–6.
- [31] Ovcharenko A, Halperin G, Etsion I. In situ and real-time optical investigation of junction growth in spherical elastic–plastic contact. *Wear* 2008;264:1043–50.
- [32] Brizmer V, Kligerman Y, Etsion I. The effect of contact conditions and material properties on the elasticity terminus of a spherical contact. *Int J Solids Struct* 2006; 43:5736–49.

- [33] Brizmer V, Zait Y, Kligerman Y, Etsion I. The effect of contact conditions and material properties on elastic-plastic spherical contact. *J Mech Mater Struct* 2006;1: 865–79.
- [34] Zait Y, Kligerman Y, Etsion I. Unloading of an elastic–plastic spherical contact under stick contact condition. *Int J Solids Struct* 2010;47:990–7.
- [35] Jackson RL, Ghaednia H, Pope S. A solution of rigid–perfectly plastic deep spherical indentation based on slip-line theory. *Tribol Lett* 2015;58:47.
- [36] Zhou K, Dong Q. A three-dimensional model of line-contact elastohydrodynamic lubrication for heterogeneous materials with inclusions. *Int J Appl Mech* 2016;8: 1650014.
- [37] Dong Q, Zhou K. Numerical modeling of elastohydrodynamic lubrication in point or line contact for heterogeneous elasto-plastic materials. *Mech Adv Mater Struct* 2016;1–9.
- [38] Dong Q, Zhou K, Chen WW, Fan Q. Partial slip contact modeling of heterogeneous elasto-plastic materials. *Int J Mech Sci* 2016;114:98–110.
- [39] Olsson E, Larsson PL. On force–displacement relations at contact between elastic–plastic adhesive bodies. *J Mech Phys Solids* 2013;61:1185–201.
- [40] Lan H, Venkatesh TA. On the relationships between hardness and the elastic and plastic properties of isotropic power-law hardening materials. *Philos Mag* 2014;94: 35–55.
- [41] Zhao JH, Nagao S, Zhang ZL. Loading and unloading of a spherical contact: from elastic to elastic–perfectly plastic materials. *Int J Mech Sci* 2012;56:70–6.
- [42] Zhao B, Zhang S, Wang QF, Zhang Q, Wang P. Loading and unloading of a power-law hardening spherical contact under stick contact condition. *Int J Mech Sci* 2015; 94–95:20–6.
- [43] Brake MRW. An analytical elastic plastic contact model with strain hardening and frictional effects for normal and oblique impacts. *Int J Solids Struct* 2015;62: 104–23.
- [44] Ferjaoui A, Yue T, Abdel Wahab M, Hojjati-Talemi R. Prediction of fretting fatigue crack initiation in double lap bolted joint using Continuum Damage Mechanics. *Int J Fatigue* 2015;73:66–76.
- [45] Beheshti A, Khonsari M. A thermodynamic approach for prediction of wear coefficient under unlubricated sliding condition. *Tribol Lett* 2010;38:347–54.
- [46] Xu H, Komvopoulos K. Fracture mechanics analysis of asperity cracking due to adhesive normal contact. *Int J Fract* 2013;181:273–83.
- [47] Sun Y, Voyiadjis GZ, Hu W, Shen F, Meng Q. Fatigue and fretting fatigue life prediction of double-lap bolted joints using continuum damage mechanics-based approach. *Int J Damage Mech* 2016. 1056789516641481.
- [48] Lemaitre J, Chaboche J-L. *Mechanics of solid materials*. Cambridge university press; 1994.
- [49] Shen F, Voyiadjis G, Hu W, Meng Q. Analysis on the fatigue damage evolution of notched specimens with consideration of cyclic plasticity. *Fatigue & Fract Eng Mater Struct* 2015;38:1194–208.
- [50] Shen F, Hu W, Meng Q. A non-local approach based on the hypothesis of damage dissipation potential equivalence to the effect of stress gradient in fretting fatigue. *Int J Fatigue* 2016;90:125–38.
- [51] De Vree J, Brekelmans W, Van Gils M. Comparison of nonlocal approaches in continuum damage mechanics. *Comput Struct* 1995;55:581–8.
- [52] Warhadpande A, Sadeghi F, Kotzalas MN, Doll G. Effects of plasticity on subsurface initiated spalling in rolling contact fatigue. *Int J Fatigue* 2012;36:80–95.
- [53] Armstrong PJ, Frederick C. A mathematical representation of the multiaxial Bauschinger effect. Central Electricity Generating Board [and] Berkeley Nuclear Laboratories, Research & Development Department; 1966.
- [54] Chaboche J, Rousselier G. On the plastic and viscoplastic constitutive equations—Part I: rules developed with internal variable concept. *J Press Vessel Technol* 1983;105:153–8.
- [55] Chaboche J-L, Rousselier G. On the plastic and viscoplastic constitutive equations—Part II: application of internal variable concepts to the 316 stainless steel. *J Press Vessel Technol* 1983;105:159–64.
- [56] Zhang T, McHugh PE, Leen SB. Finite element implementation of multiaxial continuum damage mechanics for plain and fretting fatigue. *Int J Fatigue* 2012;44:260–72.
- [57] Hojjati-Talemi R, Wahab MA. Fretting fatigue crack initiation lifetime predictor tool: using damage mechanics approach. *Tribol Int* 2013;60:176–86.
- [58] Chaboche J, Lesne P. A non-linear continuous fatigue damage model. *Fatigue & Fract Eng Mater Struct* 1988;11:1–17.
- [59] Marmi AK, Habraken AM, Duchene L. Multiaxial fatigue damage modelling at macro scale of Ti–6Al–4V alloy. *Int J Fatigue* 2009;31:2031–40.
- [60] Yuan H, Xu Y. Fracture mechanics assessment of stress concentrations in incomplete fretting contacts. *Eng Fract Mech* 2009;76:2344–58.
- [61] Lemaitre J, Desmorat R. *Engineering damage mechanics: ductile, creep, fatigue and brittle failures*. Springer Science & Business Media; 2005.
- [62] Kang G, Liu Y, Ding J, Gao Q. Uniaxial ratcheting and fatigue failure of tempered 42CrMo steel: damage evolution and damage-coupled visco-plastic constitutive model. *Int J Plasticity* 2009;25:838–60.
- [63] Lemaitre J. Coupled elasto-plasticity and damage constitutive equations. *Comput Methods Appl Mech Eng* 1985;51:31–49.
- [64] Mu Y, Liu M, Zhao Y. Numerical investigation on the elastic–plastic transition of a cylindrical coating/substrate composite under normal compression. *RSC Adv* 2017; 7:15527–35.
- [65] Version A. 6.13, analysis User's manual. Providence, RI: Dassault Systemes Simulia Corp; 2013.
- [66] Shen F, Hu W, Meng Q. A damage mechanics approach to fretting fatigue life prediction with consideration of elastic–plastic damage model and wear. *Tribol Int* 2015;82(Part A):176–90.
- [67] Santus C, Taylor D. Physically short crack propagation in metals during high cycle fatigue. *Int J Fatigue* 2009;31:1356–65.
- [68] Green I. Poisson ratio effects and critical value in spherical and cylindrical Hertzian contacts. *Appl Mech Eng* 2005;10:451.
- [69] Hibbit H, Karlsson B, Sorensen E. ABAQUS user manual, version 6.12. 2012. Simulia, Providence, RI.
- [70] Wu A, Shi X, Polycarpou AA. An elastic-plastic spherical contact model under combined normal and tangential loading. *J Appl Mech* 2012;79:051001.